



# CHIME/FRB Detection of the Original Repeating Fast Radio Burst Source FRB 121102

A. Josephy<sup>1,2</sup>, P. Chawla<sup>1,2</sup>, E. Fonseca<sup>1,2</sup>, C. Ng<sup>3</sup>, C. Patel<sup>1,2</sup>, Z. Pleunis<sup>1,2</sup>, P. Scholz<sup>4</sup>, B. C. Andersen<sup>1,2</sup>, K. Bandura<sup>5,6</sup>, M. Bhardwaj<sup>1,2</sup>, M. M. Boyce<sup>7</sup>, P. J. Boyle<sup>1,2</sup>, C. Brar<sup>1,2</sup>, D. Cubranic<sup>8</sup>, M. Dobbs<sup>1,2</sup>, B. M. Gaensler<sup>3,9</sup>, A. Gill<sup>3,9</sup>, U. Giri<sup>10,11</sup>, D. C. Good<sup>8</sup>, M. Halpern<sup>12</sup>, G. Hinshaw<sup>12</sup>, V. M. Kaspi<sup>1,2</sup>, T. L. Landecker<sup>4</sup>, D. A. Lang<sup>10</sup>, H.-H. Lin<sup>13</sup>, K. W. Masui<sup>14,15</sup>, R. Mckinven<sup>3,9</sup>, J. Mena-Parra<sup>14</sup>, M. Merryfield<sup>1,2</sup>, D. Michilli<sup>1,2</sup>, N. Milutinovic<sup>4,12</sup>, A. Naidu<sup>1,2</sup>, U. Pen<sup>13</sup>, M. Rafiei-Ravandi<sup>10</sup>, M. Rahman<sup>3</sup>, S. M. Ransom<sup>16</sup>, A. Renard<sup>3</sup>, S. R. Siegel<sup>1,2</sup>, K. M. Smith<sup>10</sup>, I. H. Stairs<sup>8</sup>, S. P. Tendulkar<sup>1,2</sup>, K. Vanderlinde<sup>3,9</sup>, P. Yadav<sup>8</sup>, and A. V. Zwaniga<sup>1,2</sup>

<sup>1</sup> Department of Physics, McGill University, 3600 rue University, Montréal, QC H3A 2T8, Canada

<sup>2</sup> McGill Space Institute, McGill University, 3550 rue University, Montréal, QC H3A 2A7, Canada

<sup>3</sup> Dunlap Institute for Astronomy and Astrophysics, University of Toronto, 50 St. George Street, Toronto, ON M5S 3H4, Canada

<sup>4</sup> Dominion Radio Astrophysical Observatory, Herzberg Astronomy & Astrophysics Research Centre, National Research Council of Canada, P.O. Box 248, Penticton, BC V2A 6J9, Canada

<sup>5</sup> CSEE, West Virginia University, Morgantown, WV 26505, USA

<sup>6</sup> Center for Gravitational Waves and Cosmology, West Virginia University, Morgantown, WV 26505, USA

<sup>7</sup> Department of Physics and Astronomy, University of Manitoba, Allen Building, Winnipeg, MB R3T 2N2, Canada

<sup>8</sup> Department of Physics & Astronomy, University of British Columbia, 6224 Agricultural Road, Vancouver, BC V6T 1Z1, Canada

<sup>9</sup> Department of Astronomy and Astrophysics, University of Toronto, 50 St. George Street, Toronto, ON M5S 3H4, Canada

<sup>10</sup> Perimeter Institute for Theoretical Physics, 31 Caroline Street N, Waterloo, ON N2L 2Y5, Canada

<sup>11</sup> Department of Physics and Astronomy, University of Waterloo, Waterloo, ON N2L 3G1, Canada

<sup>12</sup> Department of Physics and Astronomy, University of British Columbia, 6224 Agricultural Road, Vancouver, BC V6T 1Z1, Canada

<sup>13</sup> Canadian Institute for Theoretical Astrophysics, University of Toronto, 60 St. George Street, Toronto, ON M5S 3H8, Canada

<sup>14</sup> MIT Kavli Institute for Astrophysics and Space Research, Massachusetts Institute of Technology, 77 Massachusetts Avenue, Cambridge, MA 02139, USA

<sup>15</sup> Department of Physics, Massachusetts Institute of Technology, 77 Massachusetts Avenue, Cambridge, MA 02139, USA

<sup>16</sup> NRAO, 520 Edgemont Road, Charlottesville, VA 22903, USA

Received 2019 June 8; revised 2019 June 21; accepted 2019 June 23; published 2019 September 5

## Abstract

We report the detection of a single burst from the first-discovered repeating fast radio burst (FRB) source, FRB 121102, with the Canadian Hydrogen Intensity Mapping Experiment (CHIME) telescope, which operates in the frequency band 400–800 MHz. The detected burst occurred on 2018 November 19 and its emission extends down to at least 600 MHz, the lowest frequency detection of this source yet. The burst, detected with a significance of  $23.7\sigma$ , has fluence  $12 \pm 3$  Jy ms and shows complex time and frequency morphology. The 34 ms width of the burst is the largest seen for this object at any frequency. We find evidence of subburst structure that drifts downward in frequency at a rate of  $-3.9 \pm 0.2$  MHz ms<sup>-1</sup>. Our best fit tentatively suggests a dispersion measure of  $563.6 \pm 0.5$  pc cm<sup>-3</sup>, which is  $\approx 1\%$  higher than previously measured values. We set an upper limit on the scattering time at 500 MHz of 9.6 ms, which is consistent with expectations from the extrapolation from higher-frequency data. We have exposure to the position of FRB 121102 for a total of 11.3 hr within the FWHM of the synthesized beams at 600 MHz from 2018 July 25 to 2019 February 25. We estimate on the basis of this single event an average burst rate for FRB 121102 of 0.1–10 per day in the 400–800 MHz band for a median fluence threshold of 7 Jy ms in the stated time interval.

*Unified Astronomy Thesaurus concepts:* [Radio bursts \(1339\)](#); [Radio transient sources \(2008\)](#)

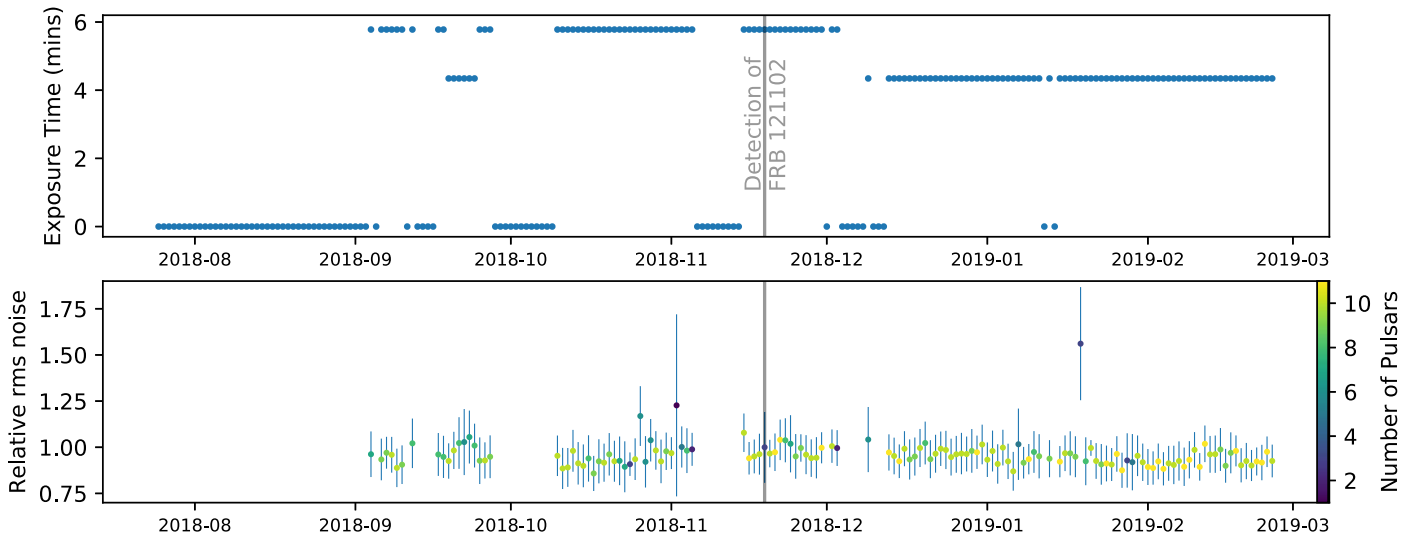
## 1. Introduction

Fast radio bursts (FRBs) are a recently recognized astrophysical phenomenon (Lorimer et al. 2007) consisting of short (few millisecond) bursts of radio waves coming from apparently cosmological distances. Their physical nature is as yet unknown.

A major clue to the FRB puzzle came with the discovery of the first repeating source, FRB 121102 (Spitler et al. 2014, 2016). Its repeating nature enabled its interferometric localization and the identification of a host dwarf galaxy at redshift  $z = 0.2$  (Chatterjee et al. 2017; Tendulkar et al. 2017). FRB 121102 is also remarkable for its sometimes complex burst phenomenology (Scholz et al. 2016; Hessels et al. 2019), which involves highly variable spectra and sub-bursts that appear to drift downward in radio frequency with time. The repetition also allows studies of burst properties in different wavebands. Until now, all such observations have been carried out at radio frequencies above 1 GHz, with bursts detected as high as 8 GHz (Gajjar et al. 2018; Michilli et al. 2018).

Of key interest is the environment around FRB 121102. Michilli et al. (2018) showed that the source has an exceptionally high Faraday rotation measure ( $\sim 10^5$  rad m<sup>-2</sup>), indicating extreme magnetoionic surroundings. This plus a persistent, variable continuum radio source co-located with FRB 121102 (Chatterjee et al. 2017; Marcote et al. 2017) has inspired a model involving a young magnetar in an expanding supernova remnant (Metzger et al. 2017, 2019; Margalit & Metzger 2018) that potentially explains many of the observed properties.

One important property is the source's scattering time, which has imprinted information on the distribution of ionized matter along the line of sight. Until now, the bursts have shown no evidence of the expected temporal asymmetry associated with multipath scattering, with an upper limit on pulse broadening of 1.5 ms at 1.5 GHz (Spitler et al. 2016). On the other hand, observations at 5 GHz have measured a scintillation bandwidth that is consistent with a scatter-broadening time of 24  $\mu$ s at



**Figure 1.** Timeline of CHIME/FRB’s daily exposure to FRB 121102 within the FWHM of the telescope’s synthesized beams at 600 MHz. The reduction in daily exposure starting 2018 December 7 is due to the failure of the computing node responsible for processing one of the four FFT-formed beams through which the source transits. The rms noise is estimated relative to that for the day of detection of the FRB 121102 burst using pulsars detected by CHIME/FRB with the marker colors denoting the number of pulsars used for the estimate. The errors on the relative rms noise account only for the day-to-day sensitivity variation and are not representative of the overall error on the fluence threshold. See Section 2.5 for a description of how the fluence threshold and the corresponding error were determined.

1 GHz (Michilli et al. 2018). So low a scattering time suggests that bursts from FRB 121102 may be detectable in the LOFAR band, despite no bursts having been seen thus far (Houben et al. 2019). However, Masui et al. (2015), for a different FRB, measured a scatter-broadening time near 800 MHz that is inconsistent with that inferred from the event’s scintillation bandwidth, i.e., two scattering timescales for one FRB. This demonstrates the existence of two distinct scattering screens toward that source, a situation that could also be true for FRB 121102. A measurement of scatter broadening would therefore be interesting, but requires a detection below 1 GHz.

Here we report the detection of a single burst from FRB 121102 in the frequency range 400–800 MHz using the Canadian Hydrogen Intensity Mapping Experiment (CHIME) telescope and its FRB detection system (CHIME/FRB Collaboration et al. 2018). We also report on data from the CHIME/Pulsar instrument, obtained simultaneously with CHIME/FRB, in which the burst also appears.

## 2. Observations and Analysis

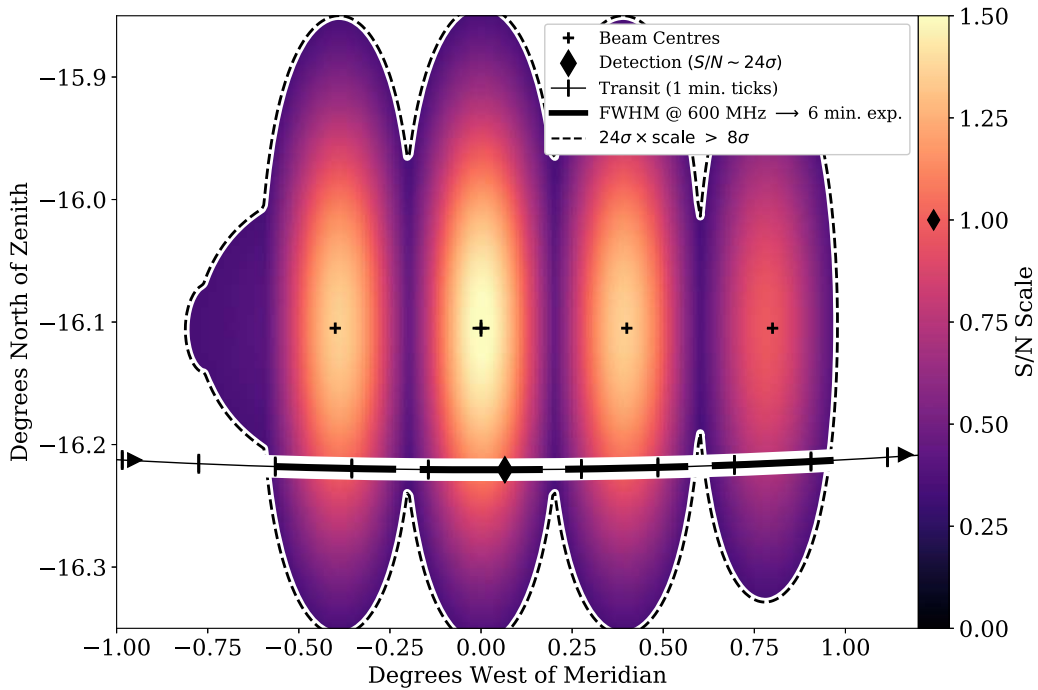
### 2.1. CHIME/FRB Detection

The CHIME/FRB instrument has been described in an overview paper in which the CHIME telescope, FRB detection instrument, and pipeline are described in detail (CHIME/FRB Collaboration et al. 2018). During the interval from 2018 July 25 to 2019 February 25, CHIME was in a commissioning state in which various components of the instrument were being tested, with software and calibration systems being updated and improved frequently. Although the CHIME/FRB system was operational starting 2018 July 25, the beam configuration for the months of July and August rendered FRB 121102 undetectable as it did not transit within the FWHM region of any of the fast Fourier transform (FFT)-formed beams at 600 MHz. Following a system reconfiguration on 2018 September 4, we were sensitive to FRB 121102 for a total of 11.3 hr, as shown in Figure 1. We truncate our reported exposure on 2019 February 25, when we brought the CHIME/FRB system down

for pipeline updates and testing. The telescope sensitivity was known to be varying from day to day during the interval due primarily to changing gain calibration strategies, but also due to a variety of issues that, once recognized, were rectified. Overall, we determine the median sensitivity to be  $7_{-4}^{+7}$  Jy ms, for a burst width of 34 ms (see Section 2.3), during on times shown in Figure 1. Further details regarding the sensitivity estimate are provided below (see Section 2.5).

The burst was detected and associated with FRB 121102 by our automated FRB detection pipeline on 2018 November 19, at 09:38:47.706 UTC (topocentric, 600 MHz), when our threshold for saving buffered intensity data was signal-to-noise ratio (S/N),  $S/N = 10$ . The nominal pipeline detection S/N for the event was 23.7, and so intensity data were saved. The event was detected in a single beam whose central pointing position is consistent with the known position of FRB 121102 (Chatterjee et al. 2017), as shown in Figure 2. This, and the similarity in nominal pipeline DM of  $565 \text{ pc cm}^{-3}$  to previously published values ( $\sim 559 \text{ pc cm}^{-3}$ ; Scholz et al. 2016), assured us of the event’s identification.

The saved intensity data, having 16k frequency channels each at 0.983 ms time resolution, allowed us to produce a “waterfall plot,” as shown in Figure 3. A complex burst morphology is seen, both in time and in radio frequency. Note that correcting for CHIME’s bandpass response is a work in progress, and is complicated by a declination-dependent  $\sim 30$  MHz ripple due to multiple reflections, declination-specific  $\sim 7$  MHz ripple due to FFT beamforming (Ng et al. 2017), as well as additional rippling due to the use of a polyphase filterbank algorithm and FFT upchannelization for defining our frequency channels (CHIME/FRB Collaboration et al. 2018). Bandpass-calibrated data are shown in the bottom subplots of Figure 3. The conversion from instrumental units to fluence is discussed in Section 2.4. Emission is clearly detected down to  $\sim 600$  MHz, by far the lowest yet seen for this source. Moreover, it also appears to be band-limited, with no emission seen below this value, in spite of good sensitivity down to 400 MHz.



**Figure 2.** Detection location and transit sensitivity for FRB 121102. The color scale reflects sensitivity variation in the four beams relevant for detection. Crosses indicate beam centers, with the largest cross denoting the detection beam center. The true location at the time of burst detection is indicated with a diamond. Protrusions on the left are caused by east–west aliasing of the synthesized beams on the right. The intersection of the transit with the FWHM at 600 MHz for each beam (indicated with thick black lines) is used for exposure calculations.

## 2.2. CHIME/Pulsar Detection

The CHIME X-Engine, in addition to supplying data to the CHIME/FRB instrument as described in CHIME/FRB Collaboration et al. (2018), also provides tied-array formed-beam data products to a separate backend that is used for targeted observations of pulsars and other known radio transients. This instrument, CHIME/Pulsar, is described in detail in Ng et al. (2018). CHIME/Pulsar has been monitoring the position of FRB 121102 reported in Chatterjee et al. (2017) since 2018 November 3. Each observation tracks the position of the source for about 19 minutes as it drifts over the meridian FOV of CHIME. All together, 23.86 hr were spent on source, covering a total of 81 days of transits up until 2019 March 1. The data were coherently dedispersed to a  $DM^{17}$  of  $558.1 \text{ pc cm}^{-3}$  then saved as a total-power filterbank time series, with a time resolution of  $327.68 \mu\text{s}$  and 1024 frequency channels each with a width of 390 kHz. Offline, a PRESTO-based (Ransom 2011) single-pulse search was conducted on these data. Throughout this period, only one burst was observed, on 2018 November 19, for which the CHIME/FRB has a simultaneous detection. The waterfall plot of this burst is shown in Figure 3. This burst was detected with an S/N of 17 using the CHIME/Pulsar instrument, and shows temporal structure similar to previous bursts of FRB 121102. We note that the S/N reported from the Pulsar backend is lower than that from the FRB backend. The difference is likely due to imperfect scaling from floating point precision to the 4-bit integer VDIF output in the early commissioning data of the Pulsar backend. For this reason, we restrict further analysis and

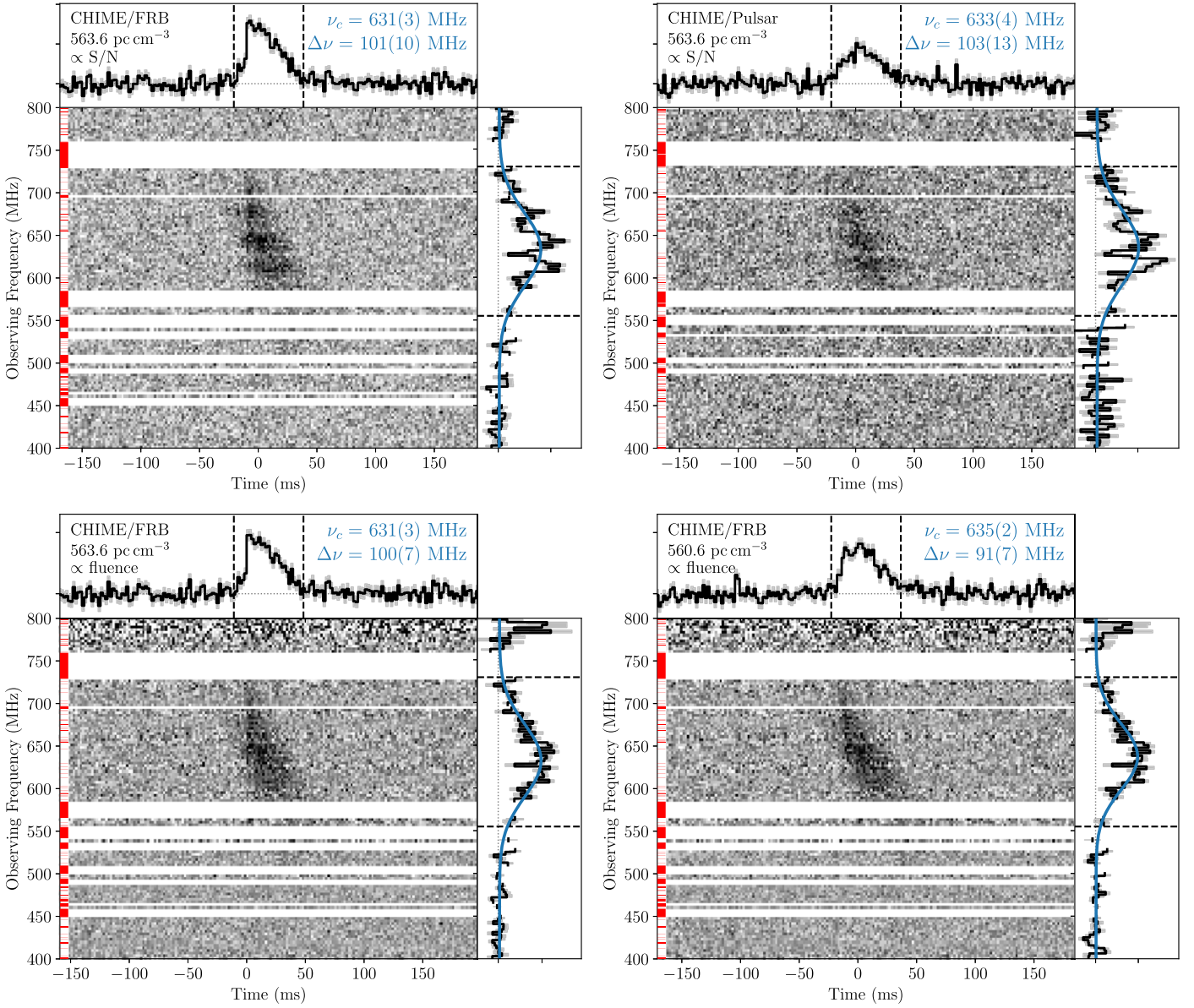
rate estimates to the FRB backend, where defining a fluence completeness limit throughout our quoted exposure is more tractable.

## 2.3. Burst Morphology Analysis

The observed burst morphology—broad pulse structure with several apparent components—might be caused by a combination of subburst drifting and scattering. To try to disentangle the two, we analyzed the CHIME/FRB intensity data first by assuming all morphology is caused by subburst drifting, and then by fitting a model burst that includes both subbursts and scattering.

To characterize subburst drifting in the burst, we optimized the DM for burst structure by finding the DM that maximizes the forward derivative of the dedispersed time series, following Hessels et al. (2019) and Gajjar et al. (2018), as shown in Figure 4. We calculated the DM transform for 400 steps ranging from 556 to 574  $\text{pc cm}^{-3}$  and smoothed the transform with a  $3 \times 3$  ( $2.8 \text{ ms} \times 0.135 \text{ pc cm}^{-3}$ ) rectangular kernel to reduce the noise. Then, we calculated the forward derivative and smoothed the resulting image further by a  $3 \times 5$  ( $2.8 \text{ ms} \times 0.225 \text{ pc cm}^{-3}$ ) rectangular kernel. Finally, we summed the absolute value of the forward derivative to the power  $n \in (1, 2, 4)$  over the time axis. The approach of Gajjar et al. (2018) corresponds to  $n = 1$ , while Hessels et al. (2019) use  $n = 2$ . We find that higher values of  $n$  select for singular sharp rises in the pulse profile, while lower values may favor multiple lower-amplitude peaks. For a given  $n$ , the maximum of a high-order polynomial fit to the curve is taken as the structure-optimizing DM. To estimate uncertainties, we normalize the DM transform such that each pixel represents an S/N value, then perform a Monte Carlo simulation by perturbing the transform with normally distributed noise. For  $n = 4$ , we find a structure-optimizing DM of  $563.6 \pm 0.5 \text{ pc cm}^{-3}$ , while  $n = 2$  gives  $565 \pm 1 \text{ pc cm}^{-3}$ . We adopt the former value as the curve

<sup>17</sup> This DM was chosen ahead of time based on previously published values (e.g., Scholz et al. 2016). The difference compared to our newly measured value is sufficiently small that it does not affect the CHIME/Pulsar pulse profile given the narrow channel widths.



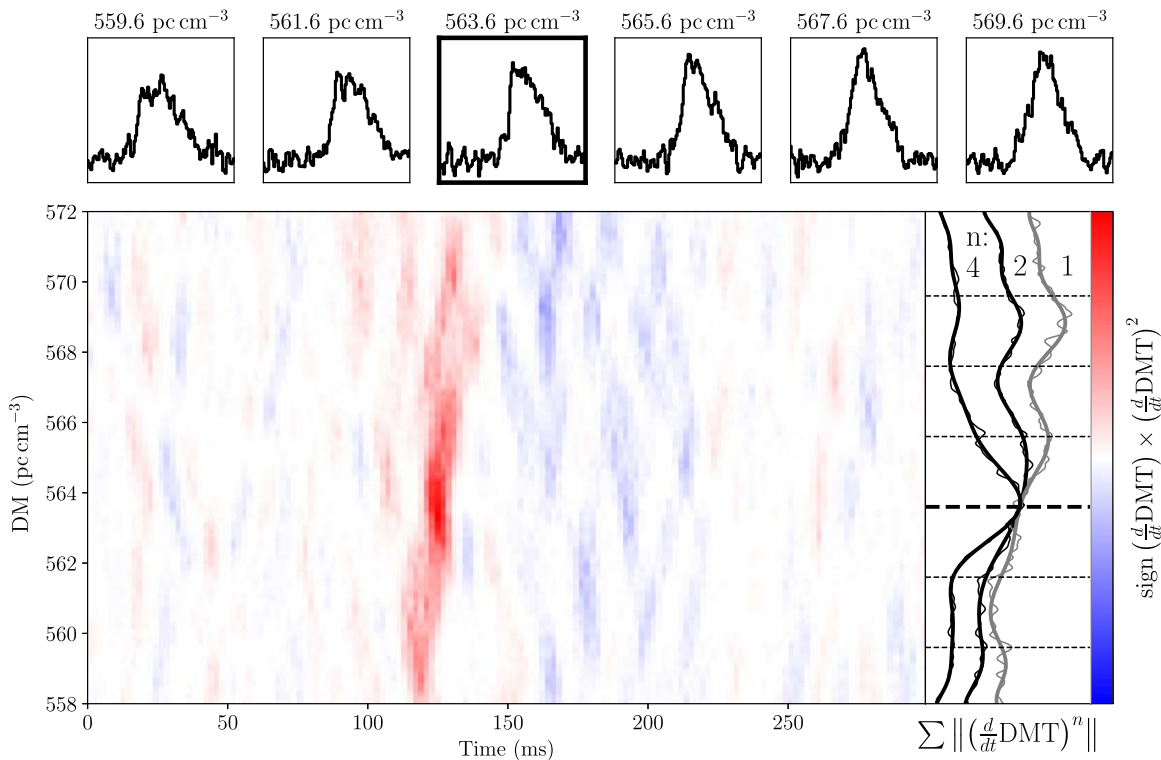
**Figure 3.** Signal intensity as a function of frequency and time (“waterfall”) plot of the CHIME/FRB (upper-left and lower subplots) and CHIME/Pulsar (upper-right subplot) detections of FRB 121102. Data have been dedispersed to the structure-optimizing DM of  $563.6 \text{ pc cm}^{-3}$ , except for the lower right subplot, which is dedispersed to the nominal 2016 September value of  $560.6 \text{ pc cm}^{-3}$  (Spitler et al. 2016). Data plotted here are downsampled to a frequency resolution of  $\sim 3 \text{ MHz}$  and a time resolution of  $\sim 2 \text{ ms}$ . For the upper subplots, the grayscale reflects S/N of the source dynamic spectrum without explicit bandpass correction. Each channel is independently normalized according to statistics of the off-pulse regions (delineated by vertical dashed lines in top panel). In the lower subplots, bandpass calibration has been applied, and the grayscale reflects fluence. Note that bandpass correction is a work in progress and is complicated by multiple factors—see the text for details. The red lines at the left sides of plots represent radio frequencies masked prior to analysis, while horizontal white stripes show the full extent of frequencies removed after all interference rejection. The right panel is the projected on-pulse spectrum. Strong (order 1) instrumental variations in bandpass are visible in the uncorrected subplots. The blue line is the best single-Gaussian fit to the spectrum (annotated with center frequency and FWHM). The top panel contains the total pulse profile after summing over the frequency channels that bracket the burst (delineated with horizontal dashed lines in the right panel; 550–730 MHz).

for  $n = 4$  has an unambiguous peak. This is several DM units higher than earlier reported DMs for this source (e.g., Spitler et al. 2016; Hessels et al. 2019) but is consistent with measurements of the structure-optimizing DM in Arecibo observations near 1.4 GHz from 2018 November (A. Seymour et al. 2019, in preparation).

Using the structure-optimizing DM, we analyze the autocorrelation of the emission region in the dedispersed dynamic spectrum, as shown in Figure 5. To mitigate RFI masking effects, we limit the analysis to the relatively clean 580–725 MHz band, which contains the majority of the observed signal (see Figure 3). The 2D autocorrelation shows

where the burst has the most self-similarity. A tilt in the ellipse reflects the subburst drift rate and here we find a rate  $-3.9 \pm 0.2 \text{ MHz ms}^{-1}$ . Assuming the pulse profile and spectral bandwidth of the burst envelope and subbursts are reasonably well described by Gaussian profiles, we measure their FWHMs from the standard deviation  $\sigma$  of a Gaussian profile fit to the summed autocorrelation over the respective axes.<sup>18</sup> We find a burst envelope width of  $33.7 \pm 0.6 \text{ ms}$  and a

<sup>18</sup> As the autocorrelation of a Gaussian profile has an FWHM  $\sqrt{2}$  times the original width and the FWHM of a Gaussian is  $2\sqrt{\ln 2} \sigma$ , we have  $\text{FWHM}_{\text{burst}} = 2\sqrt{\ln 2} \sigma_{\text{corr}}$ .



**Figure 4.** Structure-optimizing DM method. The main panel shows the signed square ( $n = 2$ ) of the forward time derivative of the smoothed DM transform (DMT), where the color scale reflects the local steepness of frequency-averaged burst profiles for different DMs. While absolute values are taken for the final metric, we show the sign to highlight rising and falling regions. Likewise, we show  $n = 2$  to highlight structure beyond a singular sharp rise. The curves in the right panel are high-order polynomial fits to time-averaged time derivatives to the power  $n$ , normalized to DM  $563.6 \text{ pc cm}^{-3}$ . Dashed lines correspond to the DMs used to produce the six frequency-averaged burst profiles at the top, with the structure-optimizing DM indicated in bold. Note that the profiles have been convolved with a 3 ms boxcar to match the smoothing used on the DM transform prior to taking the time derivative.

typical subburst width of  $26.9 \pm 0.3$  ms. The total emission bandwidth is  $87 \pm 1$  MHz and the subburst bandwidth  $71 \pm 2$  MHz. We note that bandpass correction is a work in progress, imposes structure on comparable scales, but which is stable on the timescale of the burst. The 530–580 MHz range, excluded due to significant RFI contamination, may hide additional structure and lead to an underestimated envelope bandwidth and duration. This possibility is supported by the Gaussian fit to the full-band spectrum (see Figure 3), which is centered at 631 MHz. Note that due to the limited S/N of the detection, coupled with imperfect bandpass correction, the intrinsic structure of the burst remains mostly unresolved—despite time resolutions much finer than the envelope width.

In order to quantify frequency-dependent scattering in the burst, we also applied an S/N-optimizing routine to our raw total-intensity data that uses a least-squares algorithm similar to that used in the analysis of the first 13 FRBs discovered by CHIME/FRB (CHIME/FRB Collaboration et al. 2019a). This algorithm was modified to allow for fitting an arbitrary number of Gaussian spectral components and their respective parameters against 16k-channelized dynamic spectra; per-component parameters include an arrival time, time/frequency Gaussian widths, signal amplitude, and central frequency of peak emission. The DM and scattering parameters are applied to all substructure components as “global” fit parameters.

We find that three Gaussian components are statistically favored for FRB 121102 when using the spectrum-fitting algorithm on our bandpass-calibrated data, and weighting spectra residuals by per-channel variances. In these fits, we hold the DM fixed to the structure-optimizing value of

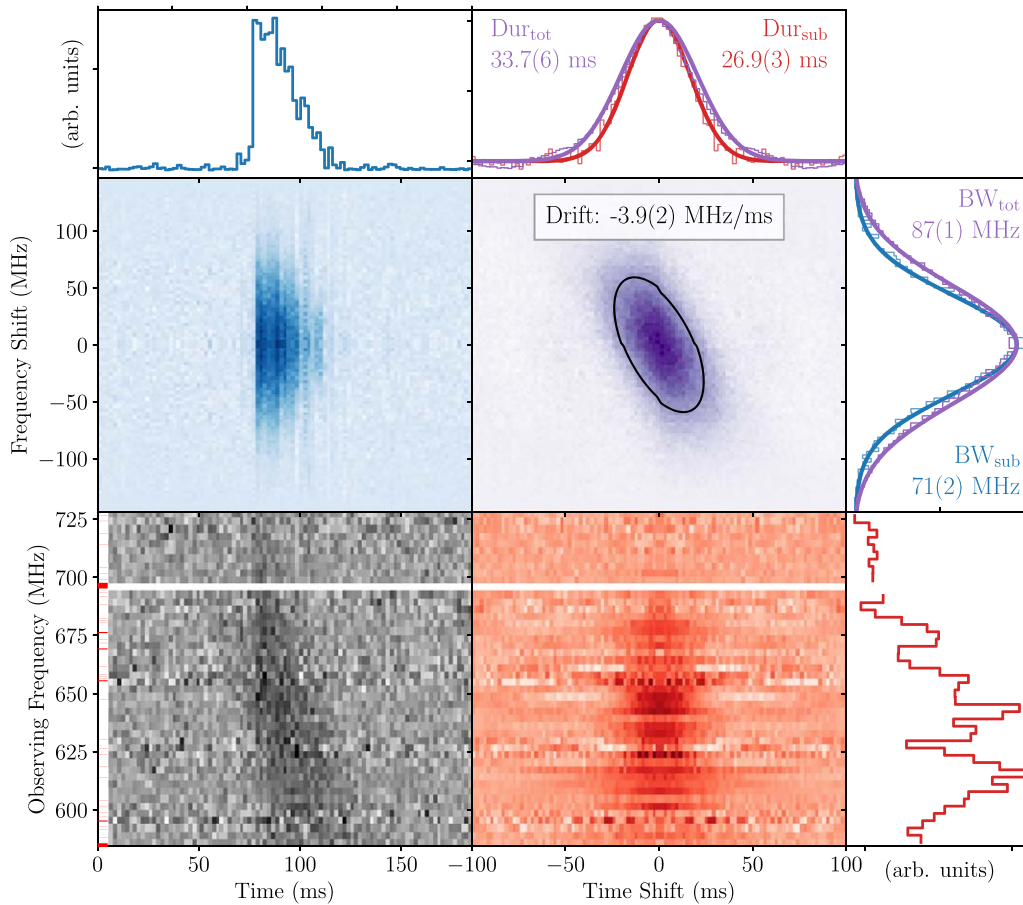
$563.6 \text{ pc cm}^{-3}$ , as well as the DM and scattering indices fixed to  $-2$  and  $-4$ , respectively. We detect no significant scattering of the burst, with a  $3\sigma$  upper limit on the scattering timescale of 9.6 ms at 500 MHz. Fit parameters are listed in Table 1.

The best-fit parameters of the three Gaussian components can also be used to constrain the subburst drift rate in time and frequency. Using these data, we find the drift rate between the three components to be  $-2.9 \pm 1.0 \text{ MHz ms}^{-1}$  when using an orthogonal-distance-regression method for weighting fits by the uncertainties in spectral and temporal centroid positions of the three components. This rate is consistent with the estimate from the model-independent autocorrelation analysis.

We note that the S/N of our data and the complex bandpass function do not allow us to robustly search for evidence of diffractive scintillation in the spectrum.

#### 2.4. Burst Fluence Determination

The burst was detected during the commissioning phase of the CHIME/FRB system. We therefore adopt the same method to estimate its fluence as in CHIME/FRB Collaboration et al. (2019a). We used the observation of 3C 48 (which has a decl. within  $0.1^\circ$  of FRB 121102) on 2019 November 18 for calibration and obtained a flux conversion factor as a function of radio frequency to account for the telescope primary beam. We assessed the uncertainty on the fluence in the same way as described in CHIME/FRB Collaboration et al. (2019a). Here, we used nine bright sources within  $1^\circ$  (instead of  $5^\circ$ ) elevation angle. Since we estimated an uncertainty on the flux as a function of frequency using the calibration sources, we have an upper and lower bound for each intensity value in the



**Figure 5.** Autocorrelations of the burst emission region. Bottom left (gray): the dedispersed dynamic spectrum with a frequency resolution of  $\sim 3$  MHz and time resolution of  $\sim 3$  ms (corrected for the effective bandpass). Bottom right (red): the 1D autocorrelation of every time series shows the characteristic width of the subbursts for different frequencies. Top left (blue): the 1D autocorrelation of every spectrum shows the characteristic subburst bandwidth for different times. Top right (purple): the 2D autocorrelation shows the self-similarity of the burst and the subburst drift rate, obtained by fitting a 2D Gaussian (FWHM indicated in black). Summed autocorrelations, with colors corresponding to the images, are shown in the panels on top and at the right. Note that structure in the projected 1D time autocorrelation is largely instrumental.

**Table 1**  
Best-fit Gaussian Components for Dynamic-spectrum Substructure

Parameter	Global Parameters		
Dispersion Measure (pc $\text{cm}^{-3}$ )	563.6		
Dispersion Index	-2		
Scattering Timescale (ms; referenced to 1 GHz)	0.27(11)		
Scattering Index	-4		
Parameter	Component 1	Component 2	Component 3
Arrival time relative to first component (ms)	0(2)	8(2)	27(2)
Amplitude (Jy)	0.6(2)	2.4(3)	0.7(4)
Time Width (ms)	3.1(5)	10.1(9)	7(2)
Frequency Width (MHz)	26(4)	33(4)	18(8)
Frequency of Peak Emission	684(4)	644(6)	612(10)

**Note.** Quoted uncertainties represent 68.3% confidence intervals. Values that were fixed during model fit are listed without uncertainties.

band-averaged profile, hence, an upper and a lower bound profile. We measured the uncertainty on the burst fluence by measuring the average area between the two profiles. Since we

were operating in a commissioning phase, a large fraction of the bandwidth was unusable for estimating the fluence for the same reasons described in CHIME/FRB Collaboration et al. (2019a). Overall, we estimated the burst fluence to be  $12 \pm 3$  Jy ms, measured over an effective total bandwidth of 255 MHz in the range 400–800 MHz. We stress that uncertainty in our fluence measurement is systematics dominated, and is expected to improve as our beam model and calibration techniques mature. The detection S/N ( $23.7\sigma$ ) should be taken as the best representation of detection significance.

### 2.5. System Sensitivity Estimate

In determining sensitivity to FRB 121102 over the course of our exposure, we characterize three potential sources of variability: (i) day-to-day instrument gain variations, (ii) changing source position within the synthesized beams, and (iii) different emission bandwidths and frequency centers within the instrument bandpass.

To capture (i), the day-to-day gain variation, we identified Galactic radio pulsars within  $5^\circ$  decl. of the source, which were detected by CHIME/FRB on at least 20% of the days between 2018 July 25 and 2019 February 25. For the purpose of this analysis, we identify a pulsar detection as robust if at least five pulses with S/N  $> 8$  were observed on each day within the FWHM region for the FFT-formed beams at 600 MHz. We use

the distribution of measured S/N values for these pulses to estimate the rms radiometer noise,  $T_{\text{sys}} / (G \sqrt{n_p \Delta \nu t_{\text{samp}}})$ , where  $T_{\text{sys}}$  is the system temperature,  $G$  is the telescope gain,  $n_p$  is the number of summed polarizations,  $\Delta \nu$  is the bandwidth, and  $t_{\text{samp}}$  is the sampling time. In contrast to the approach used for estimating the rms noise in our previous work (CHIME/FRB Collaboration et al. 2019b), we do not directly compare the measured S/N for each pulsar with its cataloged flux density. This is to avoid underestimating the sensitivity in the presence of RFI excision algorithms that cause bright pulsars to be detected with reduced S/N or overestimating it for pulsars for which CHIME/FRB is sensitive only to the tail of the flux distribution and the cataloged flux density is not representative of that observed.

For each pulsar, we take the median of the measured S/N values on each day and account for the pulse width to estimate the ratio of the rms noise at the pulsar sky location and its flux density. Assuming that the flux distribution for each pulsar is stable in time, the daily variation in this ratio for each pulsar is due to the varying rms noise for its sky location. For each day, we normalize this ratio by dividing by its median over all days the pulsar was detected. We then perform a weighted average of the normalized ratios for all pulsars detected on each day to get the overall variation in rms noise. Performing a weighted average ensures that pulsars with less intrinsic variation dominate the resulting estimate.

For (ii), we use a beam model to estimate sensitivity variation across a single transit of FRB 121102 (see Figure 2). The frequency-dependent model includes an analytic description of the FFT-formed beams (Ng et al. 2017), as well as an approximated forward-gain description of the primary beam, which is based on ray-tracing simulations done for the CHIME Pathfinder (Bandura et al. 2014). The composite model is used to compute the band-integrated relative sensitivity between different locations within the transit.

For (iii), we recognize the significant effect of our bandpass on detectability of the variety of spectra seen in FRB 121102 bursts. To test our sensitivity to bursts with different spectral energy distributions (SEDs), we use the beam-former-to-Jansky conversion as a function of frequency that is generated from the calibration process. Multiplying this array with a simulated SED and summing across frequencies gives the expected recovered signal. We restrict this simulation to Gaussian spectral profiles, with which we convolve the conversion array to get relative S/N scale factors for different emission bandwidths and central frequencies.

We combine these three sources of variability in a Monte Carlo simulation, with each sample representing the fluence threshold for some possible burst within the defined exposure. To generate a sample, we first draw a date within the covered interval, where the probability for choosing each day is proportional to its exposure (see the upper panel of Figure 1). We then draw from a Gaussian distribution parameterized according to the relative sensitivity and uncertainty for the chosen day, as given by the pulsar study (see the lower panel of Figure 1). We then uniformly draw a position along the transit and within the FWHM at 600 MHz for the relevant beams (see Figure 2). Since our decreased exposure is caused by a node failure, the active beams, and therefore possible positions, depends on the chosen day. Once a location is chosen, we compare sensitivity to the detection location to get our second relative sensitivity factor.

Next, we uniformly draw an emission bandwidth  $\Delta \nu \in [\Delta \nu_{\text{fit}}/2, 2\Delta \nu_{\text{fit}}]$ . The bandwidth determines the range of central frequencies we consider:  $\nu \in [400 \text{ MHz} + \Delta \nu/2, 800 \text{ MHz} - \Delta \nu/2]$ . The expected S/N for this SED is divided by the expected S/N for the detection-parameterized SED to get the final relative sensitivity factor ( $\nu_{\text{fit}} = 631 \text{ MHz}$ ,  $\Delta \nu_{\text{fit}} = 100 \text{ MHz}$ ; see Figure 3).

The three factors are multiplied to get an overall relative sensitivity for the simulated sample. To translate this to a fluence threshold, we first draw an initial fluence threshold from a Gaussian distribution, which is parameterized according to the recovered S/N and measured fluence of our single detection. Scaling the fluence to a detection threshold based on the S/N assumes a linear relationship between the two, which we caution is not always a valid assumption. Finally, we divide the drawn initial fluence threshold by the overall relative sensitivity to get a fluence threshold for the simulated sample. We repeat this process a million times to build up a distribution of fluence thresholds. The median value with two-sided 90% confidence interval is  $7_{-4}^{+7} \text{ Jy ms}$ . The medians and 90% confidence intervals for the three intermediate distributions of relative sensitivity are (i)  $1 \pm 0.2$ , (ii)  $0.7 \pm 0.3$ , and (iii)  $0.9 \pm 0.2$ .

## 2.6. 400–800 MHz Rate

Using the total estimated CHIME/FRB exposure time of 11.3 hr (see Section 2) to FRB 121102 and the 90% Poisson uncertainty on the single burst detected by CHIME/FRB of 0.05–4.7 bursts, we estimate an average rate in the CHIME band of 0.1–10 bursts per day for the interval 2018 July 25 through 2019 February 25. We note that the repetition of FRB 121102 is known to be non-Poissonian (e.g., Scholz et al. 2016; Oppermann et al. 2018) so this rate should be considered a rough approximation that is averaged over periods of likely variable activity.

## 3. Discussion

We have presented the detection of a single burst from the first known repeater, FRB 121102, with CHIME/FRB and CHIME/Pulsar. The burst has interesting morphology that we have characterized above, and that we now consider in light of proposed models for the progenitor and emission mechanisms.

Our detection represents the lowest radio frequency yet at which the source has been detected. This demonstrates that any low-frequency cutoff frequency (e.g., Ravi & Loeb 2019), due, for example, to possible free-free absorption at the source, must be below  $\sim 720 \text{ MHz}$ , the lowest frequency at which we have observed signal, corrected for redshift. Tendulkar et al. (2017) estimated the ionized gas properties in the host, predicting free-free absorption to be negligible even at 100 MHz, consistent with our observation.

Our analysis of the morphologically complex burst profile (see Section 2.3) suggests a DM that is  $\sim 1\%$  higher than that previously reported. Specifically, we find for this 2018 November burst, using a structure maximization method,  $\text{DM} = 563.6 \pm 0.5 \text{ pc cm}^{-3}$ . We note that a contemporaneous measurement at 1.4 GHz finds a similar value (A. Seymour et al. 2019, in preparation). Our numbers can be compared with the lower value of  $560.5 \text{ pc cm}^{-3}$  from Hessels et al. (2019) in 2016 September.

So large an increase in DM is inconsistent with enhancements in the Milky Way electron column depth, as inferred from the much smaller DM changes seen in Galactic radio pulsars (e.g., Petroff et al. 2013). Similarly, the IGM DM contribution seems unlikely to be so variable (Yang & Zhang 2017). It is therefore most likely that the change is local to the source. For models that postulate FRB 121102 to be a young compact object inside a supernova remnant (Piro & Gaensler 2018), the timescale for an increase in DM following the expected initial decrease depends on the nature of the progenitor star and the ambient density. We note that, in general, the expected rates of increase predicted by Piro & Gaensler (2018) are significantly smaller than what we have observed. Metzger et al. (2019), in their synchrotron maser model, predict stochastic DM variations from within the remnant, a result of temporary increases from bursts that follow major flares from the central engine (in their case, a young magnetar). Due to Compton scattering, however, they argue that these high DM events should be detectable preferentially at higher radio frequencies. This is at odds with our lower-frequency measurement, unless contemporaneous higher-frequency measurements find an even higher DM. On the other hand, an apparently increasing DM could be a result of intervening ejecta clumps passing through our line of sight; if so, a subsequent decrease of similar magnitude and timescale is expected.

Evidence for spectral flattening (not for individual bursts but for the overall burst rate—a “statistical” spectral index) below 1 GHz has been reported for FRB 121102 (Gourdji et al. 2019; Houben et al. 2019). However, due to large uncertainties in the FRB 121102 burst luminosity function power-law index (Law et al. 2017; Gourdji et al. 2019) as well as the unclear and variable completeness of past searches for bursts from FRB 121102 (see Gourdji et al. 2019), we do not attempt to compare rates between samples with differing fluence thresholds. Such a comparison should be done when a large, uniform, complete sample of bursts from 1.4 GHz is available. Furthermore, the comparison should be done on samples that are contemporaneous or using a framework that takes into account the variable burst rate (e.g., Oppermann et al. 2018), as the burst arrival times of FRB 121102 are known to be non-Poissonian (Scholz et al. 2016; Spitler et al. 2016).

Burst morphology is an important aspect to consider for both emission mechanism modeling and burst detection. Bursts with peaked spectral energy distributions are common, with FRB 121102 exhibiting emission bandwidths that appear to be proportional to frequency. The seven band-limited bursts at 3 GHz from Law et al. (2017) have average fractional bandwidth  $\Delta\nu/\nu = 0.16 \pm 0.04$ , the 18 band-limited bursts at 1.4 GHz from Gourdji et al. (2019) have average fractional bandwidth  $\Delta\nu/\nu = 0.12 \pm 0.04$ , and the lone CHIME/FRB detection at 600 MHz has  $\Delta\nu/\nu \simeq 0.15$ . If similar fractional bandwidths also occur at lower frequencies, at 150 MHz we expect burst envelopes with FWHM of 20–30 MHz. Large bandwidth surveys operating at low frequencies may benefit from subband searches tuned to these expected burst bandwidths.

The subburst structure in time is also relevant for detection efforts. Depending on the number of subbursts, the S/N-versus-DM curve can peak substantially beyond reference values obtained with structure-optimizing methods. Furthermore, the curve will flatten as the number of subbursts and

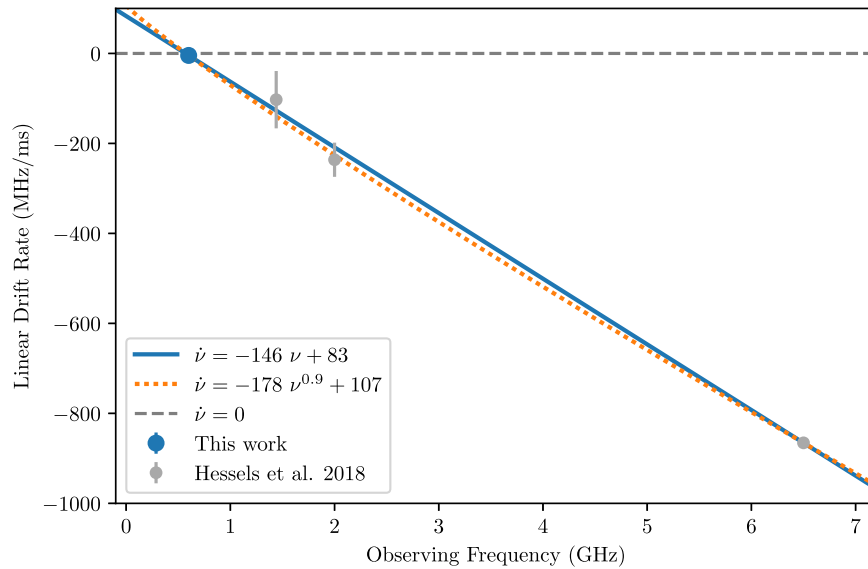
envelope width increases. As flat curves are a characteristic feature of narrowband RFI, this effect has direct implications for targeted searches that limit DM trials and classify candidates based on S/N behavior in the DM-time plane. Very aggressive RFI excision may be preferable if the search output is heavily contaminated.

The measured linear drift rate of  $-3.9 \pm 0.2 \text{ MHz ms}^{-1}$  is consistent with the CHIME/FRB drift rates measured for the only other reported repeater, FRB 180814.J0422+73, of  $\sim -1$  and  $-6 \text{ MHz ms}^{-1}$  (CHIME/FRB Collaboration et al. 2019b). Such a burst train has low-brightness-temperature analogs in the Sun, flare stars, and planets (see Hessels et al. 2019 and references therein) and might be explained as originating from an emitting region with a gradient in plasma conditions, e.g., in the deceleration of an FRB-producing blast wave (Metzger et al. 2019) or in the propagation from high- to low-curvature regions of bunches of charged particles (Wang et al. 2019). These models generally do not explicitly justify the seemingly disconnected subbursts in downward drifting bursts yet, but derive a relation  $\dot{\nu}_{\text{obs}} \propto \nu_{\text{obs}}^\alpha$ , with  $\alpha$  depending on the specifics of the progenitor model.

In Figure 6, we compare our measured FRB 121102 burst drift rate and rates for events from this source measured at 1.4–6.5 GHz. A linear drift rate evolution ( $\alpha = 1$ ) of  $\sim -150 \text{ MHz ms}^{-1} \text{ GHz}^{-1}$  with an offset of  $\sim 80 \text{ MHz ms}^{-1}$  fits the observed drift rates well, but no direct relation between  $\dot{\nu}$  and  $\nu$  can be drawn. Leaving the power-law index free, the data favor  $\alpha \sim 1$  with similar slope and intersection as the fit with fixed index. Assuming burst components are extended as has so far been observed (order 100 MHz and 1 ms) the maximum observable linear drift rate for a given data set is approximately the frequency bandwidth BW divided by the time resolution  $t_s$ , while the minimum observable drift rate is dominated by the frequency channel bandwidth  $\Delta f_c$  (although besides component widths, the sensitivity to drift rates also largely depends on the number of components and their S/N). CHIME/FRB (BW = 400 MHz;  $t_s \sim 1$  ms) is thus sensitive to linear drift rates up to  $\sim -400 \text{ MHz ms}^{-1}$  and from the Arecibo and GBT data sets ( $\Delta f_c \sim 1$  MHz) drift rates as low as  $\sim -1 \text{ MHz ms}^{-1}$  would likely be measurable—making all observations sensitive to a wide range of linear drift rates. If the apparent linear trend in Figure 6 were to hold down to the LOFAR band, the drifting rate would naively be positive,  $+61 \text{ MHz ms}^{-1}$  at 150 MHz. This would be difficult to observe if bursts have small fractional bandwidths as discussed above, and certainly if bursts are heavily scattered as expected in the LOFAR band.

The upper limit on the scattering time at 500 MHz (Section 2.3) in our burst detection implies a  $3\sigma$  upper limit of 0.6 ms at 1 GHz, which is unremarkable in the FRB population (see, e.g., CHIME/FRB Collaboration et al. 2019a). Indeed, this upper limit is significantly higher than the scattering time measurements we have made for other CHIME/FRB events. Relevant here is subburst structure and the overall width of the FRB 121102 burst we have detected, 34 ms, much greater than those of our other reported FRBs, for which much shorter scattering times were measurable. In any case, our upper limit at 1 GHz is two orders of magnitude higher than the scattering time at 1 GHz ( $24 \mu\text{s}$ ) inferred from the scintillation bandwidth at 5 GHz (Michilli et al. 2018), and provides no evidence for a second screen as observed, e.g., by Masui et al. (2015).





**Figure 6.** Comparison of FRB 121102’s CHIME/FRB burst drift rate with rates measured by Hessels et al. (2019) at higher observing frequencies. Where multiple bursts are detected with the same instrument (at 1.4 and 2.0 GHz), the weighted average and standard deviation are taken at the central frequencies of the receiver bandwidth and error bars reflect the scatter in the measurements, while the error bars at 600 MHz and 6.5 GHz reflect the measurement errors. Over this frequency range, the drift rate evolves roughly linearly with  $\sim -150 \text{ MHz ms}^{-1} \text{ GHz}^{-1}$ .

#### 4. Conclusions






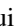


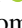



We have detected a single burst from the original repeating FRB 121102 using the commissioning CHIME/FRB system. Our detection represents the lowest radio frequency at which the source has yet been detected,  $\sim 600$  MHz. The burst has complex morphology and shows no evidence for scattering, but tentatively appears to be at a DM that is  $\sim 1\%$  higher than has previously been measured. The subbursts show downward drifting in radio frequency that has now been observed in many FRB 121102 bursts as well as in a second repeating source (CHIME/FRB Collaboration et al. 2019b). Considering previously reported drift rates in FRB 121102 bursts at different frequencies, we note a possible linear trend in drift rate as a function of observing frequency, similar to that expected in multiple emission models. Our estimated average burst rate for FRB 121102 during our precommissioning and commissioning phases based on this single burst is 0.1–10 per day, which is consistent with rates reported at higher radio frequencies, although we recognize the importance of comparing contemporaneous rates since the source rate varies. Fortunately, CHIME/FRB observes the source position daily so ultimately should be useful for comparing CHIME-band rates with those measured simultaneously at higher frequencies.

We are grateful for the warm reception and skillful help that we have received from the Dominion Radio Astrophysical Observatory, operated by the National Research Council Canada. The CHIME/FRB Project is funded by a grant from the Canada Foundation for Innovation 2015 Innovation Fund (Project 33213), as well as by the Provinces of British Columbia and Québec, and by the Dunlap Institute for Astronomy and Astrophysics at the University of Toronto. Additional support was provided by the Canadian Institute for Advanced Research (CIFAR), McGill University, and the McGill Space Institute via the Trottier Family Foundation, and the University of British Columbia. FRB research at the University of British Columbia is funded by an NSERC Discovery Grant and by the Canadian Institute for Advanced

Research. The Dunlap Institute is funded by an endowment established by the David Dunlap family and the University of Toronto. Research at the Perimeter Institute is supported by the Government of Canada through Industry Canada and by the Province of Ontario through the Ministry of Research & Innovation. The National Radio Astronomy Observatory is a facility of the National Science Foundation operated under cooperative agreement by Associated Universities, Inc. P.C. is supported by an FRQNT Doctoral Research Award and a Mitacs Globalink Graduate Fellowship. B.M.G. acknowledges the support of the Natural Sciences and Engineering Research Council of Canada (NSERC) through grant RGPIN-2015-05948, and of the Canada Research Chairs program. V.M.K. holds the Lorne Trottier Chair in Astrophysics & Cosmology, a Canada Research Chair, and the R. Howard Webster Foundation Fellowship of CIFAR, and receives support from an NSERC Discovery Grant and Herzberg Award, and from the FRQNT Centre de Recherche en Astrophysique du Québec. D.M. is a Banting Fellow. M.M. is supported by a NSERC Canada Graduate Scholarship. Z.P. is supported by a Schulich Graduate Fellowship. S.M.R. is a CIFAR Senior Fellow and is supported by the NSF Physics Frontiers Center award 1430284. P.S. is supported by a DRAO Covington Fellowship from the National Research Council Canada. The baseband system is funded in part by a CFI JELF award to I.H.S.

#### ORCID iDs

- A. Josephy <https://orcid.org/0000-0003-3059-6223>  
P. Chawla <https://orcid.org/0000-0002-3426-7606>  
C. Ng <https://orcid.org/0000-0002-3616-5160>  
Z. Pleunis <https://orcid.org/0000-0002-4795-697X>  
P. Scholz <https://orcid.org/0000-0002-7374-7119>  
B. C. Andersen <https://orcid.org/0000-0001-5908-3152>  
M. Bhardwaj <https://orcid.org/0000-0002-3615-3514>  
P. J. Boyle <https://orcid.org/0000-0001-8537-9299>  
C. Brar <https://orcid.org/0000-0002-1800-8233>  
D. Cubranic <https://orcid.org/0000-0003-2319-9676>  
B. M. Gaensler <https://orcid.org/0000-0002-3382-9558>

A. Gill  <https://orcid.org/0000-0002-3937-4662>  
 M. Halpern  <https://orcid.org/0000-0002-1760-0868>  
 G. Hinshaw  <https://orcid.org/0000-0002-4241-8320>  
 V. M. Kaspi  <https://orcid.org/0000-0001-9345-0307>  
 D. A. Lang  <https://orcid.org/0000-0002-1172-0754>  
 K. W. Masui  <https://orcid.org/0000-0002-4279-6946>  
 D. Michilli  <https://orcid.org/0000-0002-2551-7554>  
 M. Rahman  <https://orcid.org/0000-0003-1842-6096>  
 S. M. Ransom  <https://orcid.org/0000-0001-5799-9714>  
 S. R. Siegel  <https://orcid.org/0000-0003-2631-6217>  
 I. H. Stairs  <https://orcid.org/0000-0001-9784-8670>  
 S. P. Tendulkar  <https://orcid.org/0000-0003-2548-2926>

## References

- Bandura, K., Addison, G. E., Amiri, M., et al. 2014, *Proc. SPIE*, 9145, 914522  
 Chatterjee, S., Law, C. J., Wharton, R. S., et al. 2017, *Natur*, 541, 58  
 CHIME/FRB Collaboration, Amiri, M., Bandura, K., et al. 2018, *ApJ*, 863, 48  
 CHIME/FRB Collaboration, Amiri, M., Bandura, K., et al. 2019a, *Natur*, 566, 230  
 CHIME/FRB Collaboration, Amiri, M., Bandura, K., et al. 2019b, *Natur*, 566, 235  
 Gajjar, V., Siemion, A. P. V., Price, D. C., et al. 2018, *ApJ*, 863, 2  
 Gourdji, K., Michilli, D., Spitler, L. G., et al. 2019, *ApJL*, 877, L19  
 Hessels, J. W. T., Spitler, L. G., Seymour, A. D., et al. 2019, *ApJL*, 876, L23  
 Houben, L. J. M., Spitler, L. G., ter Veen, S., et al. 2019, *A&A*, 623, A42  
 Law, C. J., Abruzzo, M. W., Bassa, C. G., et al. 2017, *ApJ*, 850, 76  
 Lorimer, D. R., Bailes, M., McLaughlin, M. A., Narkevic, D. J., & Crawford, F. 2007, *Sci*, 318, 777  
 Marcote, B., Paragi, Z., Hessels, J. W. T., et al. 2017, *ApJL*, 834, L8  
 Margalit, B., & Metzger, B. D. 2018, *ApJL*, 868, L4  
 Masui, K., Lin, H.-H., Sievers, J., et al. 2015, *Natur*, 528, 523  
 Metzger, B. D., Berger, E., & Margalit, B. 2017, *ApJ*, 841, 14  
 Metzger, B. D., Margalit, B., & Sironi, L. 2019, *MNRAS*, 485, 4091  
 Michilli, D., Seymour, A., Hessels, J. W. T., et al. 2018, *Natur*, 533, 182  
 Ng, C., et al. CHIME/Pulsar Collaboration 2018, in IAU Symp. 337, Pulsar Astrophysics—The Next 50 Years, ed. P. Weltevrede (Cambridge: Cambridge Univ. Press), 179  
 Ng, C., Vanderlinde, K., Paradise, A., et al. 2017, in Proc. XXXIInd General Assembly and Scientific Symp. Int. Union of Radio Science (URSI GASS), ed. R. Stone (Piscataway, NJ: IEEE), 2946  
 Oppermann, N., Yu, H.-R., & Pen, U.-L. 2018, *MNRAS*, 475, 5109  
 Petroff, E., Keith, M. J., Johnston, S., van Straten, W., & Shannon, R. M. 2013, *MNRAS*, 435, 1610  
 Piro, A. L., & Gaensler, B. M. 2018, *ApJ*, 861, 150  
 Ransom, S. 2011, PRESTO: PulsAR Exploration and Search Toolkit, Astrophysics Source Code Library, ascl:1107.017  
 Ravi, V., & Loeb, A. 2019, *ApJ*, 874, 72  
 Scholz, P., Spitler, L. G., Hessels, J. W. T., et al. 2016, *ApJ*, 833, 177  
 Spitler, L. G., Cordes, J. M., Hessels, J. W. T., et al. 2014, *ApJ*, 790, 101  
 Spitler, L. G., Scholz, P., Hessels, J. W. T., et al. 2016, *Natur*, 531, 202  
 Tendulkar, S. P., Bassa, C. G., Cordes, J. M., et al. 2017, *ApJL*, 834, L7  
 Wang, W., Zhang, B., Chen, X., & Xu, R. 2019, *ApJL*, 876, L15  
 Yang, Y.-P., & Zhang, B. 2017, *ApJ*, 847, 22